Monthly Notices
of the
ROYAL ASTRONOMICAL SOCIETY

MNRAS **449,** L132–L136 (2015) doi:10.1093/mnrasl/slv032

On the origin of γ-ray emission in η Carina

S. Ohm,[1⋆] V. Zabalza,[2] J. A. Hinton[2,3] and E. R. Parkin[4]

[1]*DESY, D-15738 Zeuthen, Germany*
[2]*Department of Physics and Astronomy, The University of Leicester, University Road, Leicester LE1 7RH, UK*
[3]*Max Planck Institut für Kernphysik, Heidelberg D-69029, Germany*
[4]*School of Physics and Astronomy, University of Leeds, Woodhouse Lane, Leeds LS2 9JT, UK*

Accepted 2015 February 13. Received 2015 February 13; in original form 2015 January 28

ABSTRACT

η Car is the only colliding-wind binary for which high-energy γ rays are detected. Although the physical conditions in the shock region change on time-scales of hours to days, the variability seen at GeV energies is weak and on significantly longer time-scales. The γ-ray spectrum exhibits two features that can be interpreted as emission from the shocks on either side of the contact discontinuity. Here, we report on the first time-dependent modelling of the non-thermal emission in η Car. We find that emission from primary electrons is likely not responsible for the γ-ray emission, but accelerated protons interacting with the dense wind material can explain the observations. In our model, efficient acceleration is required at both shocks, with the primary side acting as a hadron calorimeter, whilst on the companion side acceleration is limited by the flow time out of the system, resulting in changing acceleration conditions. The system therefore represents a unique laboratory for the exploration of hadronic particle acceleration in non-relativistic shocks.

Key words: radiation mechanisms: non-thermal – stars: individual: η Car.

1 INTRODUCTION

Particle acceleration up to very high energies in pulsar wind nebulae and supernova remnants is well established, with non-thermal emission seen from radio to TeV energies. The mechanism of diffusive shock acceleration (DSA; e.g. Drury 1983) is usually invoked to explain the non-thermal emission in these systems, suggesting that all systems with strong shocks accelerate particles. The shocks present in some Galactic colliding-wind binaries (CWBs) – binary systems with two massive stars and powerful winds – seem to satisfy all the criteria for particle acceleration and detectable high-energy emission: shock velocities of $\gtrsim$1000 km s^{-1}, available wind power of $\sim 10^{37}$ erg s^{-1} and copious targets for the production of high-energy radiation: soft photon fields and high-density gas. Indeed non-thermal radio emission from some CWBs has been seen (e.g. De Becker 2007), and models predicting emission at γ-ray energies from such systems developed (e.g. Eichler & Usov 1993; Benaglia & Romero 2003; Bednarek 2005; Reimer, Pohl & Reimer 2006). Only recently, however, has strong experimental evidence appeared for γ-ray emission from such systems: in the unique case of η Car, using *AGILE* (Tavani et al. 2009) and *Fermi*-LAT (Abdo et al. 2009). A hard X-ray tail is also seen from η Car (Viotti et al. 2004; Leyder, Walter & Rauw 2010).

η Car is a binary system in a ∼5.5-yr orbit (Damineli et al. 2008). The masses and mass-loss rates of the stellar companions (Table 1), together with the eccentricity of the CWB ($e \approx 0.9$), make this a very unusual system. The thermal X-ray emission associated with the wind collision region (WCR) and surrounding nebula has been extremely well studied (e.g. Hamaguchi et al. 2014, and references therein) and considerable theoretical work has gone into understanding this emission (e.g. Pittard & Corcoran 2002; Parkin et al. 2011; Madura et al. 2013).

The LAT-detected emission above 200 MeV has been reported by Abdo et al. (2010), Farnier, Walter & Leyder (2011) and Reitberger et al. (2012). The high-energy γ-ray spectrum exhibits two distinct features: a low-energy component with a cutoff around 1 GeV, and a significantly harder component above ∼10 GeV. Both components are found to be variable, but on longer time-scales and less dramatically than in X-rays. Upper limits from HESS at energies above ∼500 GeV are more restrictive than the extrapolated *Fermi*-LAT flux, implying a sudden drop in γ-ray flux (Abramowski et al. 2012). The high gas densities present in the WCR of CWBs may result in the efficient production of π^0-decay γ rays (Bednarek & Pabich 2011; Farnier et al. 2011), and lead to a calorimetric situation where all energy injected into particle acceleration is radiated away on short time-scales. In addition, the two shocks in this system have very different properties, and cannot be considered as a single system (Bednarek & Pabich 2011). The acceleration and interaction of non-thermal particles in η Car has been studied in previous work (e.g. Tavani et al. 2009; Abdo et al. 2010; Bednarek & Pabich 2011; Farnier et al. 2011), but the complex geometry, and all of the relevant phase-dependent time-scales have so far not been fully considered. Here, we present a 3D dynamical model combined with particle injection, propagation and interaction used to study the origin of γ-ray emission from η Car. We consider the stellar wind

⋆ E-mail: stefan.ohm@desy.de

Table 1. Stellar parameters used throughout this work.

Parameter	Primary	Companion	Reference
$R_\star$ ($R_\odot$)	100	20	1
$T_\star$ (K)	25 800	30 000	2
$L_\star$ ($10^6\,L_\odot$)	4	0.3	2
$\dot{M}$ ($M_\odot\,yr^{-1}$)	4.8×10^{-4}	1.4×10^{-5}	3
v_∞ (km s^{-1})	500	3000	3

References: (1) Hillier et al. (2001); (2) Davidson & Humphreys (1997); (3) Parkin et al. (2009).

shocks of both stars in η Car, and model the light curve and spectra from MeV to TeV energies. We first present the geometrical model and discuss the relevant time-scales in the system before moving to the full model, results and discussion.

2 MODEL

2.1 Dynamical model

To model the non-thermal emission from η Car, we apply the dynamical model introduced in Parkin & Pittard (2008). The orbit of the two stars is calculated in the centre-of-mass frame and the stellar winds are assumed to have reached terminal velocities before they interact. Orbital and stellar parameters are given in Table 1. Two regions are defined (Parkin & Pittard 2008):

The shock cap is the region where the two stellar winds collide, and the flow accelerates outwards from the stagnation point along the contact discontinuity (CD). The *ballistic point* is defined where the flow speed reaches 85 per cent of the primary terminal wind speed. We assume radial symmetry w.r.t. to the apex, but the orbital motion introduces a skew in the orientation of the shock cap. The skew angle changes as a function of orbital phase φ, and can reach up to 38° but is well below 10° for $0.1 \lesssim \varphi \lesssim 0.9$. The shape of the shock cap, tangential velocity of the flow and surface density is determined by momentum balance of the two winds (Canto, Raga & Wilkin 1996). For 100 φ bins from $\varphi = 0.0$ to 1.0, we generate a grid of points along the shock cap. This grid is formed by 36 azimuthal and 82 radial points.

The ballistic flow is entered beyond the ballistic point, where the flow is assumed to be unaffected by the stars' gravity, ram pressure of the winds or thermal pressure in the WCR. Beyond the ballistic point, the wind material of the two stars is assumed to mix over a mixing length (see below) and to flow with a speed according to momentum balance of the two winds.

A collapse of the WCR on to the companion star or dynamical instabilities in the WCR were proposed to explain the dramatic variability seen in thermal X-rays close to periastron (e.g. Corcoran 2005; Parkin et al. 2011). The collapse is modelled by turning off particle acceleration in the inner 80 per cent of the shock cap during the X-ray minimum ($0.985 \lesssim \varphi \lesssim 1.025$).

Fig. 1 shows the overall geometry of the system, the motion of the two stars and the stagnation point of the two winds, the shock-cap size, geometry at two phases, and the line of sight to the observer (projected on to the orbital plane). The asymmetric path of the stagnation point is due to the skew of the shock cap caused by the rapid motion of the companion around periastron.

2.2 Time-scales

Several different time-scales in η Car are relevant for particle acceleration and interaction. The acceleration time $t_{\rm acc}$ of a particle

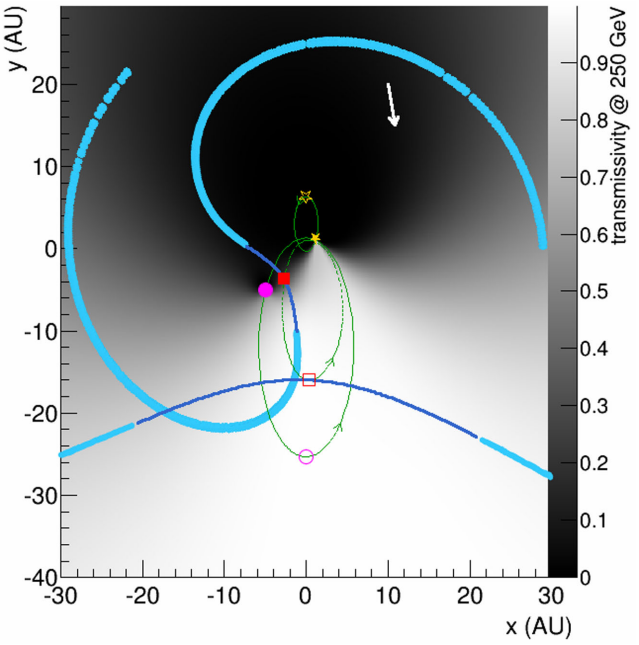

Figure 1. Geometry of the η Car system as a function of orbital phase overlaid on a transmissivity map at 250 GeV at $\varphi = 0.04$ in the plane of the two stars. The green solid, long dashed and short lines show the motions of the primary, companion and stagnation point around the centre of mass of the system. At $\varphi = 0.04$ and 0.5 the positions of these elements in the system are represented, respectively, by closed and open symbols. The position of the shock cap is indicated by a blue line, the ballistic part is shown as azure segments that show the direction of movement of each of the computational elements. The projected line of sight to the observer is shown with a thick black arrow (Madura et al. 2012).

in DSA is determined by the shock speed $v_{\rm s}$, the magnetic field strength B, and the diffusion in terms of the Bohm diffusion coefficient $\kappa = \eta_{\rm acc}\kappa_B$: $t_{\rm acc} \approx 50\,\eta_{\rm acc}\,v^{-2}_{\rm s,10^3\,km\,s^{-1}}(E_{\rm acc,GeV}/B_{\rm G})$ s.

The magnetic field of the two stars in η Car is unknown. We adopt plausible surface magnetic field strengths of 100 G (see e.g. Walder, Folini & Meynet 2012), and spatial dependence following Eichler & Usov (1993), with a toroidal form for most of the orbit and varying between ($0.1 \lesssim B \lesssim 10$) G.

The post-shock (PS) regions on both sides of the CD are very different in nature: along the entire orbit the primary shock is expected to be radiative, whereas the companion shock is adiabatic. The slow dense primary wind collapses into a thin sheet of dense material, while the gas on the companion side flows out of the system without significant cooling. We calculate the thickness of the primary PS region for a radiative shock following Zhekov & Palla (2007). For the companion side, the thickness of the PS region can be calculated from mass conservation. For the wind parameters in Table 1, the typical thickness of the companion PS region ($\sim$1 au) is orders of magnitude larger than the primary PS region ($\sim10^{-4}$ au). Note that densities in the WCR are typically 10^8 cm^{-3}(10^7 cm^{-3}) on the primary (companion) side at apastron, and an order of magnitude higher close to periastron.

Fig. 2 shows the key time-scales as a function of particle energy in the primary and companion PS regions for $\varphi = 0.05$. On both sides of the CD, electrons cool much faster than the typical time it takes gas to flow from the shock apex to the edge. Coulomb scattering dominates below 100 MeV, while inverse Compton (IC) scattering ($E_e \sim 10$ GeV) and synchrotron cooling ($E_e \gtrsim 100$ GeV) dominate at higher electron energies.

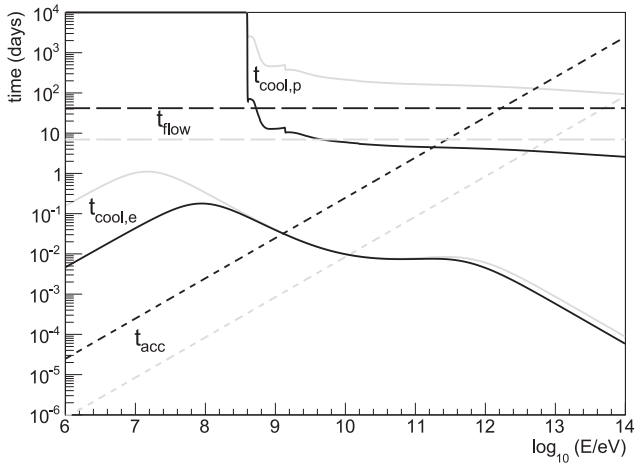

Figure 2. Key time-scales in the primary (black) and companion (grey) shocked wind. The flow time of a gas packet to reach the shock-cap edge is shown in long dashed, the acceleration time-scale in short dashed, and the cooling time-scales for electrons ($t_{\rm cool,\,e}$, Coulomb, IC, and synchrotron losses) and protons ($t_{\rm cool,\,p}$) in solid lines. $\eta_m athrmacc = 15$ is assumed in both cases.

On the primary side, the cooling time for protons is still shorter than the flow time. This suggests that for this shock an equilibrium is reached and that essentially no accelerated particles leave the shock cap. The cooling time of protons on the companion side, however, is longer than the flow time, which implies that protons are accelerated whilst moving along the shock cap and escape in to the ballistic flow. This more complex situation is treated separately in a semi-analytic model described below.

2.3 Time-dependent model

The dynamical model implies that the solid angles of the shock cap as viewed from the primary and companion stars are 1.2 and 5.2 sr, respectively. In addition, only the wind kinetic power normal to the shock will be available for particle acceleration, limiting the available power to $1.6(7.6) \times 10^{36}$ erg s^{-1} on the primary (companion) side. We model the two components of emission detected by *Fermi*-LAT as arising from the two sides of the WCR as initially suggested by Bednarek & Pabich (2011). The low-energy component, which is extremely luminous and has a cutoff around a few GeV, originates on the primary side, where the high PS density will limit particle acceleration and provide high emission efficiency through the interaction of all accelerated protons. The harder, fainter high-energy component originates on the companion side, where the lower density will allow for acceleration limited only by the flow time-scale, and result in lower luminosity due to most particles escaping without interacting. However, a certain level of mixing between the two layers of the WCR is needed to reach the detected emission levels, a phenomenon seen in hydrodynamical simulations of η Car (Parkin et al. 2011).

The faster cooling time-scales of electrons (Fig. 2), mean that much smaller values of $\eta_{\rm acc}$ are required than for protons, with super-Bohm acceleration needed for the high-energy component. Electron dominance of either component requires an electron to proton ratio of more than 1 (cf. the commonly assumed 1 per cent) due to the additional electron emission produced down to MeV energies. For these reasons, we adopt the hadronic scenario in the following.

Below we give a general description of how time-dependent particle injection and γ-ray production is treated in our model. We employ the radiative code used in Hinton & Aharonian (2007).

Primary side: acceleration of particles in the PS region of the primary is in saturation and counterbalanced by losses. The maximum energy a particle can reach depends on the exact location at which it enters the shock. Not only the magnetic field changes across the shock cap, but also the shock velocity, as the angle between stellar wind and shock cap is changing. At the same time, radiation energy densities and gas density change. To calculate the emission from the primary side of the shock cap, we calculate the tangential velocity $v_{\rm t}$ of the radiative layer for each annulus (Canto et al. 1996). The shock velocity is given by $v_{\rm s} = \frac{3}{4}\sqrt{v_{\rm prim}^2 - v_{\rm t}^2}$. Inserting $v_{\rm s}$ into $t_{\rm acc}$ and solving for the energy where $t_{\rm acc} = t_{\rm cool}$ yields the maximum particle energy in each annulus. The power available for particle acceleration $P_{\rm avail,i} = \dot{E}_{\rm avail,i}$ depends on the solid angle of the annulus, $\Omega_i = 2\pi(\cos\theta_{i-1} - \cos\theta_i)$, the primary mass-loss rate and wind speed: $P_{\rm avail,i} = \frac{1}{8\pi}\Omega_i \dot{M}_1 v_{\rm w}^2$. A constant fraction $\epsilon_{\rm p}$ of the available wind power is assumed to go into accelerated protons $P_{\rm p,\,i} = \epsilon_{\rm p} P_{\rm avail,\,i}$. From this, we calculate the CR proton injection spectrum and equilibrium γ-ray spectrum in each annulus (Ginzburg & Syrovatskii 1964; Zabalza, Paredes & Bosch-Ramon 2011). Given the high densities in the primary wind and PS region, there is an additional contribution to the high-energy γ-ray emission from charged pion decay and subsequent secondary electron emission.

Companion side: as can be seen in Fig. 2, the lower PS density on the companion side results in accelerated protons losing only a small fraction of their energy to p–p collisions in the shock cap. DSA therefore takes place under changing conditions as the relativistic particle population flows outwards in the shock cap. To approximate this acceleration, we follow the CR population through each annulus outwards on the shock cap, and apply a semi-analytic acceleration scheme as follows.

We follow the standard picture of DSA in non-relativistic shocks (Bell 1978): as particles enter the shock they are scattered from downstream to upstream by the turbulent wake and from upstream to downstream by the Alfvén waves generated by the energetic particles themselves attempting to escape upstream. After a time Δt, particles with initial energy of E_0 will have a final energy $\ln(E_{\Delta t}/E_0) = t/t_{\rm acc}$, where $t_{\rm acc} = 3\eta_{\rm acc}\kappa_{\rm B} v_{\rm s}^{-2} r(r+1)/(r-1)$, r is the shock compression ratio, and $v_{\rm s}$ is the velocity of the shock. For each crossing there is a probability $4u_2/c$, where u_2 is the downstream flow velocity, of the particles being advected downstream, resulting in a mean probability of remaining in the shock after a time Δt of $\ln(P_{\Delta t}) = -3/(r-1)\ln(E_t/E_0)$. This process results in a downstream particle distribution with a power-law index of $p_{\rm CR} = -(r+2)/(r-1)$, which under strong shock conditions ($r = 4$) results in the well-known $p_{\rm CR} = -2$ index.

We derive the relativistic particle distributions along the shock cap by, at each time step Δt, injecting a fraction $\epsilon_{\rm c}^0$ of the wind kinetic power in particles with energy $E_0 = 1$ GeV. The gain in energy due to acceleration over the time Δt is applied as above, and a fraction $(1 - P_{\Delta t})$ of the particles at each given energy are lost downstream. On subsequent steps, only the particles remaining in the shock will continue to be accelerated, whereas particles lost downstream will be advected with the annulus until the ballistic flow is reached (note that very little energy is lost in the downstream region to p–p collisions, as can be seen in Fig. 2). In addition to the energy injected in particles at E_0, additional power is required to provide the particle energy gain. For the properties of the shock

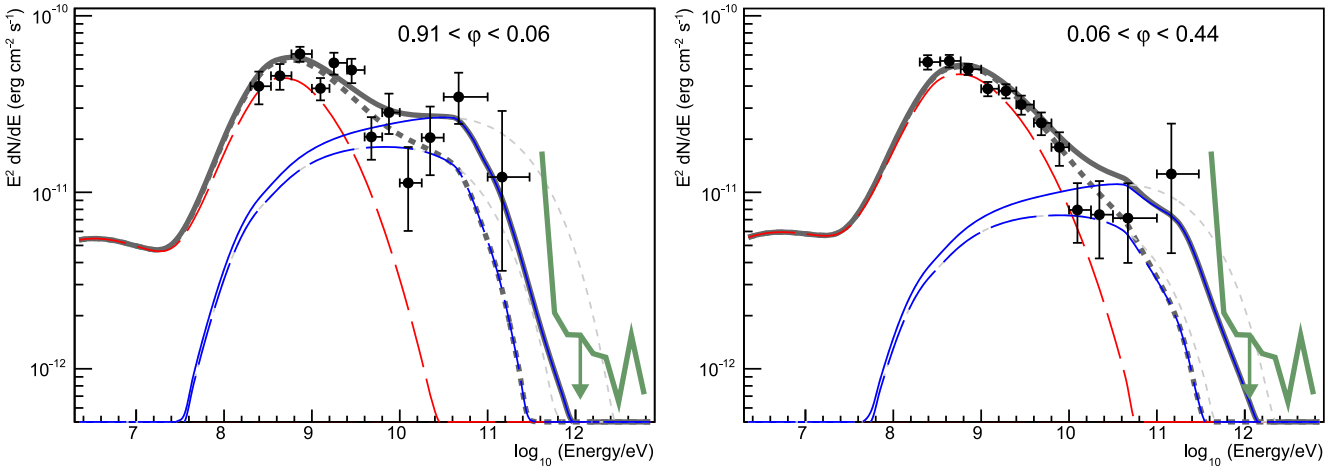

Figure 3. Model spectra and γ-ray SED for the periastron (left) and the apastron phase bin as used in Reitberger et al. (2012). Red long-dashed lines indicate the primary contribution to the emission, assuming $\eta_{\rm acc} = 15$. Solid (long-dashed) blue lines show the observed companion emission for $\eta_{\rm acc} = 5$ ($\eta_{\rm acc} = 15$), and short dashed thin grey lines show the intrinsic emission. Grey thick lines show the total emission for $\eta_{\rm acc} = 5$ (solid) and $\eta_{\rm acc} = 15$ (short dashed). TeV data are from Abramowski et al. (2012).

on the companion side of η Car, we have found that a total kinetic power fraction of $\epsilon_{\rm c} \sim 15\epsilon_{\rm c}^0$ is used for particle acceleration.

Towards the edge of the shock cap, the reduced wind ram pressure owing to shock obliquity, and the increasing CR pressure from the particles being accelerated may cause a modification of the structure of the shock, leading to non-linear effects in acceleration (see e.g. Malkov & O'C Drury 2001, for a review). To account for this effect, we adopt the semi-analytic approach of non-linear DSA by Berezhko & Ellison (1999), resulting in a hardening at the highest energies of up to $p_{\rm CR} \simeq -1.75$. A deeper study of the acceleration process in CWB, including shock modification, will be discussed in a forthcoming paper (Zabalza, Ohm & Hinton, in preparation).

Emission from the ballistic flow: given the low gas density in the companion PS region, most of the accelerated protons will not interact, but leave the shock cap in the ballistic flow. Simulations indicate that the wind material is subject to numerous instabilities and that the radiative layer of gas mixes with the wind material of the two stars (Parkin et al. 2011). We assume no mixing of the two stellar winds in the shock-cap region, but full mixing over a certain mixing length beyond the ballistic point. The two stellar winds and the radiative layer are assumed to form a region of mixed material at the edge of the shock cap at a distance r_0 from the apex of the shock with thickness d_0 and density $\rho_0 = (d_{\rm ps,\,1}\rho_1 + d_{\rm ps,\,2}\rho_2 + d_{\rm wall}\rho_{\rm wall})/d_0$. In our model mixing occurs exponentially, over a characteristic scale equal to the shock-cap radius. While moving away from the ballistic point, the density of the mixed material decreases as $(r_0/r)^2$. As the mixed material flows outwards, the two stars orbit each other and a spiral structure of dense rings will form (cf. Fig. 1). The γ-ray emission from p–p interactions in the ballistic flow is calculated in time steps much shorter than the interaction time-scale, with the emission spectrum fixed to that found for p–p emission at the shock-cap edge. We note that the diffusion time-scale out of the flow region is always much longer than the flow time-scale for the adopted value of η, the modelled B-field, and the energy range considered.

Pair-production absorption is significant for emission above ~100 GeV given the strong stellar radiation fields. We calculated the pair-production opacity (e.g. Dubus 2006) along the line of sight from each point on the shock cap and ballistic flow in each phase bin, considering the system geometry for the given phase and the density and direction of the primary and companion stellar radiation fields (with parameters as shown in Table 1). A transmission map for the orbital plane is shown in Fig. 1, showing how 250 GeV emission from behind the stars is completely suppressed.

3 RESULTS

Fig. 3 shows the γ-ray spectrum for two phase bins including (i) hadronic emission from accelerated protons on the primary and companion side, (ii) hadronic emission from protons accelerated in the companion shock and interacting in the ballistic flow, and (iii) emission from secondary electrons on the primary side. A fraction of $\epsilon_{\rm p,\,c} = 20$ per cent of the available wind power goes in to particle acceleration at both primary and companion shocks in the curves shown and different values of η are tested.

In the γ-ray light curve shown in Fig. 4 the low-energy component is dominated by the primary at almost all phases. Variability on the primary side is predicted only when the WCR collapses. For the rest of the orbit, the γ-ray emission on the primary side is constant due

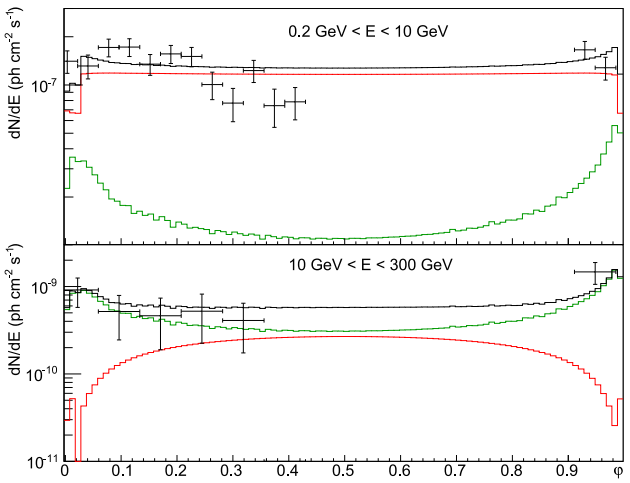

Figure 4. γ-ray light curve in the two energy bands used by Reitberger et al. (2012). Red lines show the primary contribution, green the (absorbed) companion contribution, and black the total predicted emission. $\eta = 15$ and $\epsilon = 0.2$ are used.

to the calorimetric behaviour and constant injected power. γ-ray emission from the companion side is variable over the orbit due to the changing densities in the ballistic flow. The high-energy light curve is dominated by emission from protons accelerated on the companion side that escape and interact in the ballistic flow. Some residual γ-ray emission in both components of the γ-ray spectrum are expected even during the collapse of the WCR as a result of protons interacting in the ballistic flow that have been launched at earlier phases at the ballistic point (cf. Fig. 1).

4 DISCUSSION

The model described above provides a reasonable level of agreement with the observed γ-ray light curve and spectral energy distribution (SED) of η Car. Furthermore, the broad features of the expected emission emerge from simple arguments based on the system geometry, mass flow and energetics. Consideration of the time-dependent 3D geometry of the system is, however, critical for modelling of the light curve around periastron and the impact of pair-production absorption. We have shown that inclusion of a realistic geometry is important for energetics and the relative contribution of the two shocks and that the level of emission around 1 GeV requires extremely high-efficiency γ-ray production, consistent (uniquely) with hadron calorimetry. We consider the dominance of the SED by emission from accelerated protons and nuclei to be robust. Dominance by electrons of either component is very difficult due to energy-loss time-scales and would certainly require an electron to proton ratio of >1.

ACKNOWLEDGEMENTS

We would like to thank the anonymous referee for carefully reading the manuscript, which improved the quality of the paper.

REFERENCES

Abdo A. A. et al., 2009, ApJS, 183, 46
Abdo A. A. et al., 2010, ApJ, 723, 649
Abramowski A. et al., 2012, MNRAS, 424, 128
Bednarek W., 2005, MNRAS, 363, L46
Bednarek W., Pabich J., 2011, A&A, 530, A49
Bell A. R., 1978, MNRAS, 182, 147
Benaglia P., Romero G. E., 2003, A&A, 399, 1121
Berezhko E. G., Ellison D. C., 1999, ApJ, 526, 385
Canto J., Raga A. C., Wilkin F. P., 1996, ApJ, 469, 729
Corcoran M. F., 2005, AJ, 129, 2018
Damineli A. et al., 2008, MNRAS, 384, 1649
Davidson K., Humphreys R. M., 1997, ARA&A, 35, 1
De Becker M., 2007, A&AR, 14, 171
Drury L. O., 1983, Rep. Prog. Phys., 46, 973
Dubus G., 2006, A&A, 451, 9
Eichler D., Usov V., 1993, ApJ, 402, 271
Farnier C., Walter R., Leyder J., 2011, A&A, 526, A57
Ginzburg V. L., Syrovatskii S. I., 1964, The Origin of Cosmic Rays. Macmillan, New York
Hamaguchi K. et al., 2014, ApJ, 784, 125
Hillier D. J., Davidson K., Ishibashi K., Gull T., 2001, ApJ, 553, 837
Hinton J. A., Aharonian F. A., 2007, ApJ, 657, 302
Leyder J., Walter R., Rauw G., 2010, A&A, 524, A59
Madura T. I., Gull T. R., Owocki S. P., Groh J. H., Okazaki A. T., Russell C. M. P., 2012, MNRAS, 420, 2064
Madura T. I. et al., 2013, MNRAS, 436, 3820
Malkov M. A., O'C Drury L., 2001, Rep. Prog. Phys., 64, 429
Parkin E. R., Pittard J. M., 2008, MNRAS, 388, 1047
Parkin E. R., Pittard J. M., Corcoran M. F., Hamaguchi K., Stevens I. R., 2009, MNRAS, 394, 1758
Parkin E. R., Pittard J. M., Corcoran M. F., Hamaguchi K., 2011, ApJ, 726, 105
Pittard J. M., Corcoran M. F., 2002, A&A, 383, 636
Reimer A., Pohl M., Reimer O., 2006, ApJ, 644, 1118
Reitberger K., Reimer O., Reimer A., Werner M., Egberts K., Takahashi H., 2012, A&A, 544, A98
Tavani M. et al., 2009, ApJ, 698, L142
Viotti R. F., Antonelli L. A., Rossi C., Rebecchi S., 2004, A&A, 420, 527
Walder R., Folini D., Meynet G., 2012, Space Sci. Rev., 166, 145
Zabalza V., Paredes J. M., Bosch-Ramon V., 2011, A&A, 527, A9
Zhekov S. A., Palla F., 2007, MNRAS, 382, 1124

This paper has been typeset from a TEX/LATEX file prepared by the author.